Kawamoto *et al. Earth, Planets and Space* (2016) 68:190
DOI 10.1186/s40623-016-0564-4

Earth, Planets and Space

FULL PAPER

Open Access

First result from the GEONET real-time analysis system (REGARD): the case of the 2016 Kumamoto earthquakes

Satoshi Kawamoto[1*], Yohei Hiyama[1], Yusaku Ohta[2] and Takuya Nishimura[3]

Abstract

We present the initial results of rapid fault estimations for the 2016 Kumamoto earthquake on April 16 (M_j 7.3), and coseismic displacements caused by the two large foreshocks that occurred on April 14 (M_j 6.5) and April 15 (M_j 6.4) from the GEONET real-time analysis system (REGARD), which is based on a Global Navigation Satellite System (GNSS) kinematic positioning technique. The real-time finite-fault estimate (M_w 6.85) was obtained within 1 min and converged to M_w 6.96 within 5 min of the origin time of the mainshock (M_j 7.3). The finite-fault estimate shows right-lateral strike-slip fault along the Futagawa fault segment, which is consistent with the finite-fault model inferred from post-processed GNSS and InSAR analysis. Furthermore, significant coseismic displacements were observed due to the April 14 and April 15 foreshocks at nearby sites, though these earthquakes were smaller than the pre-assigned system threshold. Our results also demonstrate the potential for the GNSS-based earthquake early warning system for inland earthquakes.

Keywords: GNSS real-time positioning, Real-time magnitude estimation, Rapid source extent estimation, The 2016 Kumamoto earthquakes

Introduction

The mainshock of the 2016 Kumamoto earthquakes (M_j 7.3) occurred at 01:25 on April 16, 2016 (Japan Standard Time, +9 GMT; hereafter the April 16 mainshock [M_j 7.3]), and two large foreshocks (M_j 6.5, M_j 6.4; hereafter the April 14 foreshock [M_j 6.5] and the April 15 foreshock [M_j 6.4]) occurred around the northern part of the Hinagu fault segment at 21:26 on April 14 (JST) and at 00:03 on April 15 (JST), respectively (Fig. 1; Japan Meteorological Agency [JMA] 2016a). These successive earthquakes occurred along the Futagawa–Hinagu fault zone, which is a well-known active fault zone in Kyushu Island of western Japan. The earthquakes caused significant damage along the fault zones: A total of 7996 houses were completely destroyed and there were 49 casualties as of June 16, 2016 (Cabinet Office 2016).

JMA issued an earthquake early warning (EEW; e.g., Hoshiba et al. 2008) of "warning level" within 10 s after the origin of the April 16 mainshock (M_j 7.3). The EEW provided the hypocenter (32.8°N, 130.8°E, 10 km), magnitude (M 7.1), and predicted seismic intensities of the earthquake (maximum seismic intensity 7; JMA 2016b) within 30 s after the origin time. This information is key for emergency responses in seconds to minutes. Subsequent reactions included rescue and evacuation plans in the severe aftershock environment. Then, the rapid characterization of both hypocenter and source extent is extremely important because earthquakes can result in secondary disasters (e.g., tsunamis, landslides, fires, and large aftershocks), which often occur just above the source area of the earthquake.

A possible technology for real-time computation of a finite-fault estimate is established using real-time Global Navigation Satellite System (GNSS) positioning technology, which provides real-time three-dimensional ground displacements (e.g., Blewitt et al. 2009; Ohta et al. 2012, 2015; Crowell et al. 2012, 2016;

*Correspondence: kawamoto-s96tf@mlit.go.jp
[1] Geodetic Observation Center, Geospatial Information Authority of Japan, 1 Kitasato, Tsukuba, Japan
Full list of author information is available at the end of the article

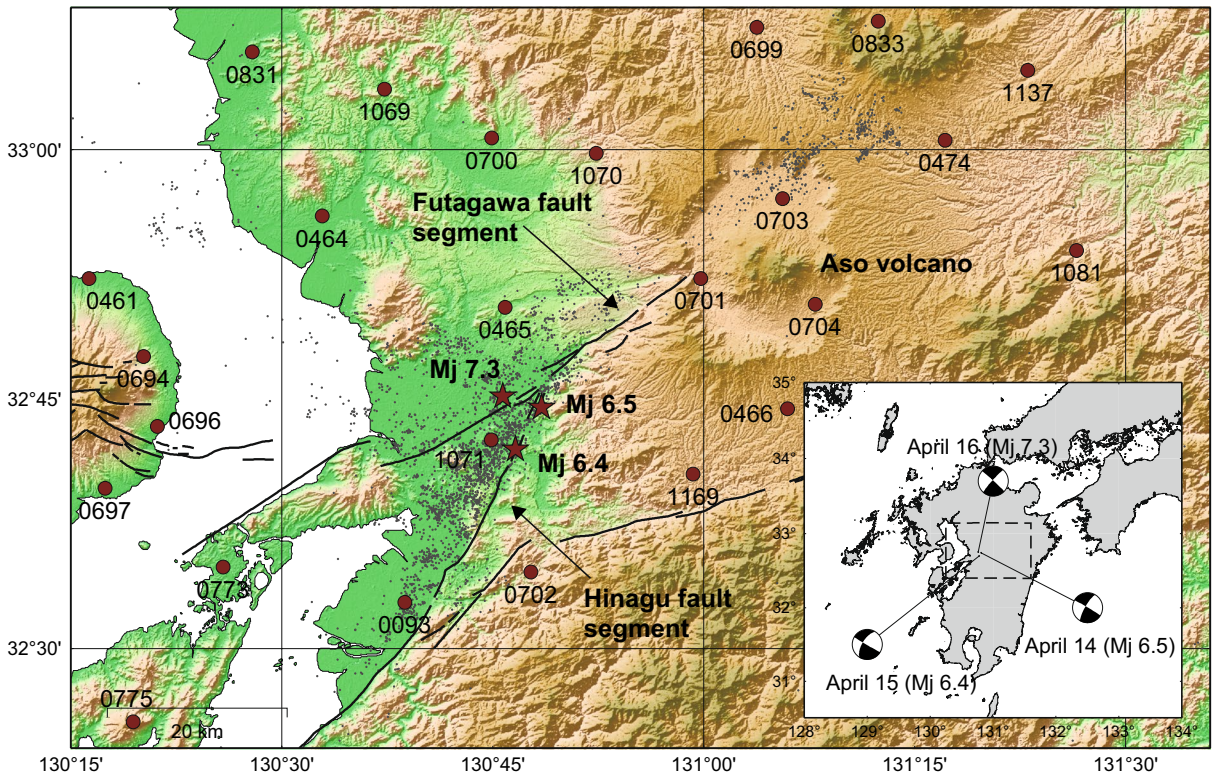

Fig. 1 Map showing the distribution of stations around the focal area. *Red circles* denote the GEONET stations. The *black dashed line* in the inset represents the study area. The *red stars* show the epicenters for the 2016 Kumamoto earthquakes, including the April 16 mainshock (M_j 7.3) and two foreshocks (M_j 6.5; M_j 6.4). The *black lines* indicate the traces of active faults (HERP 2013). *Gray dots* represent the aftershock distribution in the JMA unified hypocenter catalog between April 14, 2016, and May 18, 2016. The CMT solutions estimated by JMA are also shown in the *inset*

Grapenthin et al. 2014; Kawamoto et al. 2015; Melgar et al. 2013, 2015; Melgar and Bock 2013). The Geospatial Information Authority of Japan (GSI) has operated a continuous real-time GNSS network, named GEONET, which consists of more than 1300 stations. The real-time GEONET Analysis system for Rapid Deformation monitoring (REGARD system) using GEONET has been developed in collaboration with Tohoku University since 2012. Globally, several GNSS-based EEW systems are under operation, e.g., GlarmS in Northern California United States (US; Grapenthin et al. 2014) and G-FAST in the Pacific Northwest of the US (Crowell et al. 2016).

The primary purpose of the REGARD system is to provide unsaturated magnitude estimates for large earthquakes greater than M 8 as well as length, width, and slip amount by computing a single rectangular fault model for earthquakes with uniform slip, and slip distribution model for large interplate earthquakes with $M_w > 8$ (Kawamoto et al. 2015). Furthermore, the fault geometry of the single rectangular fault model is inverted as free parameters with loose constraints using a pre-assumed focal mechanism table as a priori information. Therefore, the system is capable of modeling events such as inland or intraplate earthquakes, which rupture unknown faults because of the fault plane cannot be exactly assumed compared with interplate earthquake. Real-time kinematic-GNSS (RTK-GNSS) may have an ability to capture the coseismic displacements due to earthquakes with $M_w > 5.5$ for near-field stations (Geng et al. 2013).

This paper presents the first operational results from the REGARD system for real earthquakes. First, we briefly introduce the procedure of the REGARD system for automatic computation of a single rectangular fault model. Second, we show actual real-time estimation results for the 2016 Kumamoto earthquakes including real-time finite-fault estimates for the April 16 mainshock (M_j 7.3) and detection of coseismic displacements observed for the two foreshocks. Finally, simulated real-time fault model estimates for the two foreshocks are shown.

Methods

REGARD: the Real-time GEONET Analysis System for Rapid Deformation monitoring

The REGARD system consists of three subsystems: the real-time positioning subsystem, the event detection

subsystem, and the fault model inversion subsystem (Fig. 2). The real-time data stream from the GEONET stations is processed by the real-time positioning subsystem using RTKLIB 2.4.2 software (Takasu 2013), and 1-Hz station positions are estimated using dual-frequency phase and pseudo-range data in real time. The predicted part of the International GNSS Service (IGS) ultra-rapid orbit (Kouba 2009) is adopted for the satellite orbit information. The elevation cutoff angle is set at 7°. The event detection subsystem detects earthquakes based on the JMA EEW and/or RAPiD algorithm (Ohta et al. 2012) with little modification; the subsystem also simultaneously uses neighboring stations as the detection threshold to reduce false detections (Kobayashi et al. 2012). If an earthquake with $M > 7.0$ is issued by the JMA EEW and/or the observed discrepancy between short-term (60 s) and long-term (600 s) averages exceeds 10 cm at three neighboring GEONET stations, an earthquake event is recognized. According to past experience, first information of $M7$-class earthquake is available in ~30 s from the JMA EEW. Then, the latest static displacements will be extracted and repeatedly modeled by a single rectangular fault with an a priori model and slip distribution along an assumed plate boundary.

The single rectangular fault modeling routine estimates 12 parameters: nine fault parameters (latitude, longitude, depth, length, width, strike, dip, rake, and slip) and a translation parameter for the east, north, and vertical directions that accounts for the common-mode noise. The translation parameters were introduced to reduce the influence of the common-mode noise caused by the reference station in RTK-GNSS processing, e.g., the model error of atmospheric delay and the coseismic displacement at the reference station. To assume a normal prior distribution for the model parameters, we adopted the inversion method proposed by Matsu'ura and Hasegawa (1987), which supposes Gaussian errors in both the observed data and prior data to incorporate prior information about model parameters into the observation data. Standard deviations of $0.02L$ (in °), $0.02L$ (in °), 5 (km), $2L$ (m), $2L$ (m), 10 (°), 10 (°), 10 (°), and 10 (m) are assumed for the nine fault parameters, where L is the initial fault length. The initial location and fault length are assumed using the location and magnitude of the JMA EEW and the scaling law of Utsu (2001): $L/W = 2$ and $s/L = 5 \times 10^{-5}$, where W is the fault width and s is the slip amount. If the JMA EEW information is unavailable, the initial location is assumed to be the position at the station where the maximum displacement is observed, and the magnitude is empirically assumed to be $M = 6.2 + 2 \log {}_{10}5d_{\max}$, where $d_{\max}$ is the maximum displacement. Strike, dip, and rake are assumed using a predetermined focal mechanism database (Fig. 3) simplified using the results of Terakawa and Matsu'ura (2009).

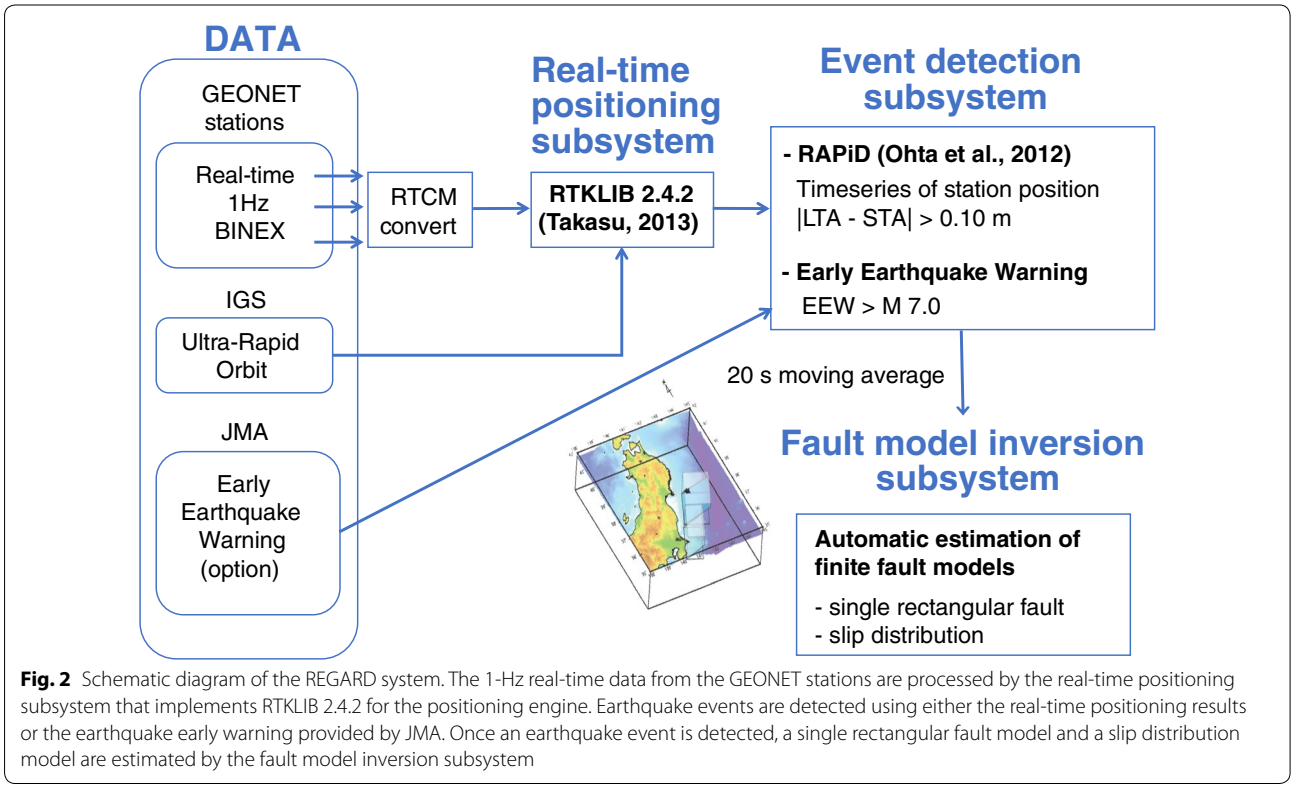

Fig. 2 Schematic diagram of the REGARD system. The 1-Hz real-time data from the GEONET stations are processed by the real-time positioning subsystem that implements RTKLIB 2.4.2 for the positioning engine. Earthquake events are detected using either the real-time positioning results or the earthquake early warning provided by JMA. Once an earthquake event is detected, a single rectangular fault model and a slip distribution model are estimated by the fault model inversion subsystem

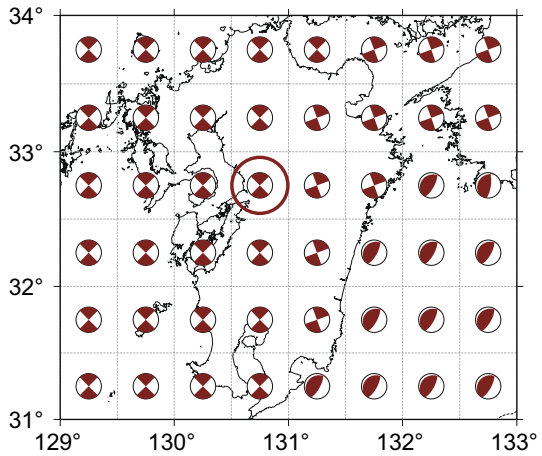

Fig. 3 Focal mechanism table used as a priori information for the inversion. The a priori strike, dip, and rake angles are assumed as the focal mechanism data nearest to the epicenter. For the inversion of the 2016 Kumamoto earthquake (M_j 7.3), the focal mechanism enclosed in a *red circle* at (32.75°N, 130.75°E) was used for the initial model

The parameters are optimized using Newton's method. The Green's function is calculated by a dislocation model in a homogeneous half-space (Okada 1992). As soon as the computation of a single rectangular fault is finished, the next inversion starts with updated static displacements. Before each inversion, the number of stations is reduced to 200 including 50 near-field stations and randomly selected 150 stations to reduce the computation time. The inversion result is evaluated by a value of variance reduction (VR) in residual sum of squares of three-dimensional displacements normalized by standard deviations. If the VR improves from the a priori model, both the model and the a priori model are modified with the new parameters. A sequence of single rectangular fault model inversions is continued for 5 min. Additional details on the inversion method are provided by Kawamoto et al. (2015).

Results and discussion

During the 2016 Kumamoto earthquakes, the REGARD system successfully estimated the single rectangular fault models for the April 16 mainshock (M_j 7.3) in real time. Furthermore, coseismic displacements could be captured by the RTK positioning results for the two foreshocks. However, real-time fault model inversions were not carried out because their magnitude and maximum displacement were lower than the assigned threshold of the system. Therefore, we show the simulation results of real-time situations with a decreased threshold of magnitude for the two foreshocks to check the performance of real-time fault modeling.

Real-time finite-fault model estimate for the April 16 mainshock (M_j 7.3)

The final fault model estimate shows a right-lateral strike-slip with northwest dip along the Futagawa fault segment of the Futagawa–Hinagu fault zone (Fig. 4, Additional files 1 and 2: Figures S1, S2). The inferred rupture extends from around the intersection between the Futagawa fault segment and the Hinagu fault segment to the western part of the caldera of the Aso volcano.

The JMA EEW system issued the first warning message within 9 s after the event origin time (01:25:05 JST), indicating a value of M 5.9, which was updated to M 7.1 in 18 s later (JMA 2016b). The magnitude issued by JMA EEW exceeded the threshold value in REGARD ($M > 7.0$); thus, the fault model inversion subsystem was automatically launched. The REGARD system started the extraction of static offsets from the estimated real-time displacement waveforms at 48 s from the origin time, which were smoothed by the application of the 20 s moving average filter, and the initial inversion was finished at 58 s. The sequence of the inversions started from the a priori location (130.8 E, 32.8 N) from the EEW message, and a priori strike, dip, and rake angles (315°, 90°, and 0°, respectively) were assumed from the pre-assumed focal mechanism database (Fig. 3).

The mainshock caused strong ground shaking, which was observed at the stations within ~100 km from the epicenter by 60 s with clear permanent displacements observed at nearby stations (Fig. 5). Some of the stations were shaking at the time 58 s, from which the initial static offsets were extracted from the real-time positioning; the ground shaking of the mainshock had decayed to the noise level at all stations within ~100 km by 120 s. Large horizontal displacements of ~96 cm to the southwest direction were observed at site 0701 and of ~75 cm to the northeast direction at site 0465 were observed. These displacements were in good agreement with the coseismic displacements later obtained from the daily coordinates of the GEONET F3 solution (Yarai et al. 2016), e.g., a horizontal displacements of ~98 cm to the southwest direction at site 0701 and of ~76 cm to the northeast direction at site 0465. The time lag between the displacements from the real-time positioning and the F3 solution is less than 1 day; thus, the contribution of early post-seismic deformation should be small. The discrepancies were less than ~2 cm, and the observed displacements were significantly larger than the measurement error.

Table 1 and Additional file 1: Figure S1 show the history of model parameter updates for single rectangular fault models. By the third inversion result, the fault model estimates yielded VR > 80% and M_w ~ 6.8 (assumed rigidity was 30 GPa). For these fault model estimates, a length of ~11 km was stably obtained, but the width ranged

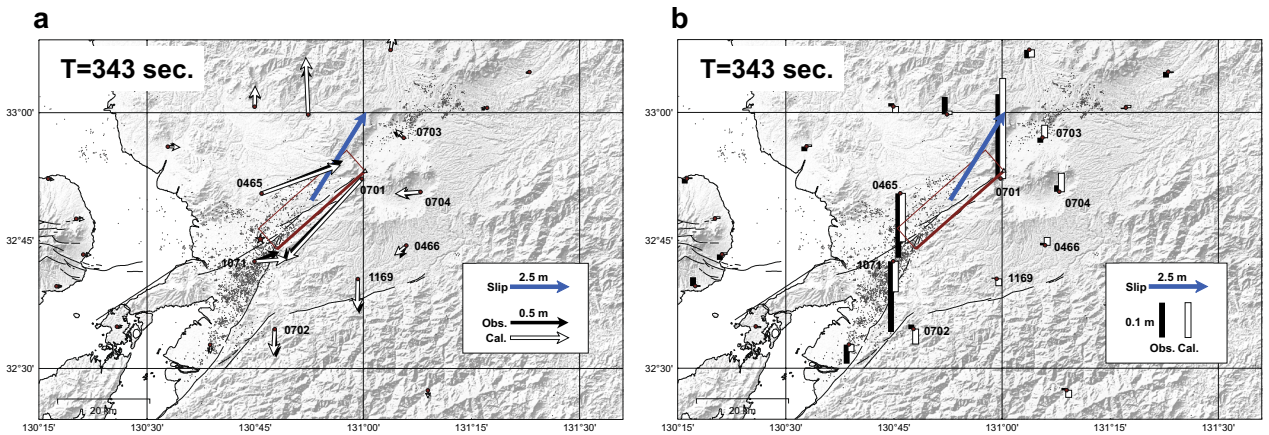

Fig. 4 Real-time finite-fault model estimation result for the 2016 Kumamoto earthquake mainshock (M_j 7.3) in 343 s after the event origin. Observed (*black arrows*) and predicted (*white arrows*) displacements for **a** horizontal and **b** vertical components. For the inversions, 200 stations were used in REGARD. The predicted displacements correspond to the final solution of the real-time fault model estimates. The *red rectangle* represents the estimated fault plane, and the *blue arrow* shows the slip vector. The epicenter of the mainshock is shown as a *red star*. The aftershocks in the JMA unified hypocenter catalog between April 14, 2016, and May 18, 2016, are shown as *gray dots*. *Black lines* indicate the ground traces of the active faults (HERP 2013)

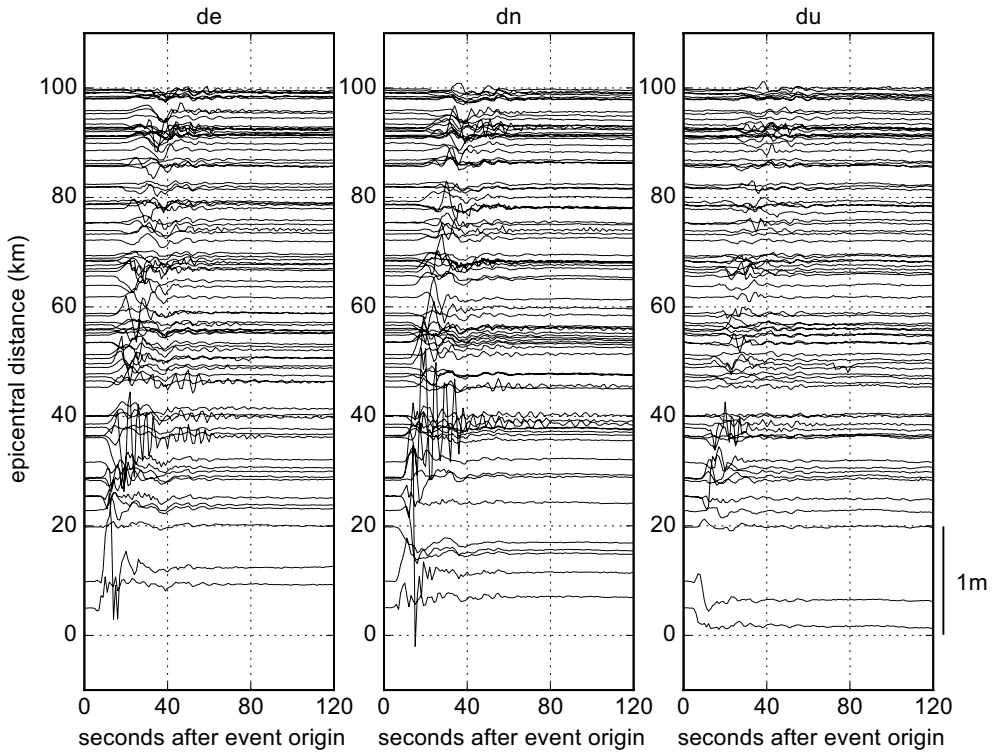

Fig. 5 Record of RTK-GNSS time series within 100 km of the epicenter obtained by REGARD after the event origin time (01:25:05 JST). The real-time displacements are estimated every second. Notable coseismic permanent displacements are also recorded at nearby sites in the focal area

from 1.4 to 6.8 km and the slip ranged from 10 to 40 m. However, the products of width and slip were approximately stable because of the relation that the ground displacements are roughly proportional to the product of width and slip. For this reason, M_w estimates were stable. From the fourth inversion result, which was obtained

Table 1 Finite-fault models computed by the REGARD system during the 2016 Kumamoto earthquake (M_j 7.3)

Model	Time	Elapsed time	Lat. (°)	Lon. (°)	Depth (km)	Length (km)	Width (km)	Strike (°)	Dip (°)	Rake (°)	Slip (m)	M_w	VR (%)
REGARD1	01:26:03	00:58	32.794	130.924	0.00	11.67	6.76	295.87	81.88	352.79	9.89	6.85	80.8
REGARD2	01:26:45	01:40	32.800	130.926	1.49	11.20	2.37	295.28	76.05	351.16	28.81	6.84	81.8
REGARD3	01:27:01	01:56	32.803	130.932	1.44	11.51	1.41	294.17	73.72	349.31	43.28	6.81	83.7
REGARD4	01:29:55	04:50	32.889	131.003	0.00	25.33	9.55	227.91	55.96	196.87	4.72	6.96	96.2
REGARD final	01:30:48	05:43	32.896	131.004	0.00	25.50	10.35	228.50	54.47	196.70	4.41	6.96	96.2
Yarai et al. (2016)		–	32.879	130.992	0.5	19.7	12.3	235	63.9	209.0	3.9	6.90	–
			32.880	130.979	2.0	4.9	6.4	52.7	65.9	190.1	3.6	6.28	
			32.786	130.811	2.0	11.0	19.9	205	69.4	178.0	2.4	6.73	

The finite-fault model consists of three rectangular fault planes (Yarai et al. 2016) is also listed for comparison. The elapsed time from the event origin time (01:25:05 on April 16, 2016 JST) is also shown. The position denotes the upper left corner of the fault plane. A variance reduction (VR) is estimated with the residual sum of squares of three-dimensional displacements normalized by standard deviations

within 5 min, VR improved to 96%, and all model parameters became very stable. The updated finite-fault estimate converged to a fault plane along the Futagawa fault segment, which was the conjugate fault plane of the previous fault model estimates. The final fault estimate was obtained after 343 s from the event origin with M_w 6.96.

The Earthquake Research Committee, Headquarters for Earthquake Research Promotion (HERP), a governmental committee that evaluates earthquake activities in Japan, reported that the 2016 Kumamoto earthquake was considered to be mainly due to the activity of the Futagawa segment (HERP 2013, 2016). Yarai et al. (2016) show an earthquake fault model inferred from the post-processed GNSS data and InSAR observations, which consists of three rectangular faults dipping northwest with right-lateral strike-slip, including a main rupture of M_w 6.90 along the Futagawa fault segment and another rupture with M_w 6.73 along the northern part of the Hinagu fault segment. A CMT solution by JMA (2016c) also shows M_w 7.0. Our final fault model estimate is in good agreement with the M_w estimates described above and is approximately consistent with the main rupture of the finite-fault model of Yarai et al. (2016) except for the strike angle and length: The strike angle was ~7° smaller and the length was ~6 km longer. These slight differences would be natural considering the simplicity of the single rectangular fault model used by the REGARD system. That is, the discrepancies may have been caused by the number of fault planes as well as the dense observation data of InSAR. Because a large part of the displacement at site 1071 is explained by the rupture along the northern part of the Hinagu fault segment, both the horizontal and vertical displacements at site 1071 were poorly explained (Fig. 4, Additional file 1: Figure S1). As a result, the strike angle deviated southward and the length was estimated to be longer.

Although the single rectangular fault model was successfully estimated within 1 min, convergence to the true fault plane required an additional 4 min. Therefore, further improvement is required to model inland earthquakes stably. Clearly, the inversion results up to the third model converged to another local minimum compared to the final result because the a priori fault plane was assumed to be the conjugate fault (Table 1). Then, the width and slip amount became unstable during the sequence of the inversions. Changes in the combination of far-field stations, which were randomly thinned out, might also have a slight influence. This instability could be avoided by comparing the VR of an inversion result using other fault planes as an a priori parameters.

For more reliable fault model estimation, we can consider the other approaches. For example, G-FAST first estimates CMT using rapidly computed static offsets to determine the fault orientation and then picks the better model between two slip distribution models on the main and auxiliary fault planes (Crowell et al. 2016). BEFORES optimizes the slip distribution together with the fault geometry using a Bayesian formulation (Minson et al. 2014). Another approach would be an inversion that tightly constrains the length and width to avoid the instability between the width and slip observed for the first three inversion results. A similar approach is employed for G-larmS, a GPS-based EEW system in northern California, which fixes the width, strike, and dip angles to the predominant seismogenic depth and faults (Grapenthin et al. 2014). For the kinematics of the fault slip, use of the seismogeodetic approach is important. The combination of high-rate GPS data and strong motion data yields high-rate displacements and velocities (e.g., Bock et al. 2011; Melgar et al. 2013). Such seismogeodetic modeling should improve the resolution and estimation stability of the coseismic fault model (Melgar and Bock 2015; Melgar et al. 2015) that should be important for more accurate GNSS-based EEW systems.

Coseismic displacements associated with the April 14 foreshock (M_j 6.5) and the April 15 foreshock (M_j 6.4)

The two large foreshocks (the April 14 M 6.5 and April 15 M 6.4 events) occurred in less than 3 h, a span of time in which it is impossible to separate individual coseismic displacements by daily analysis such as GEONET F3 solutions (Nakagawa et al. 2009). In contrast, the RTK-GNSS positioning has a great advantage for the separation of coseismic offsets of these subsequent earthquakes (e.g., Ohta et al. 2015). Although the fault model inversions were not carried out for these foreshocks in real time, real-time kinematic positioning results from the REGARD system were available, providing displacements at frequencies as high as 1 Hz. We extracted coseismic static offsets by taking the differences between the averages of 60 epochs (60 s) before and after the foreshocks. The extracted coseismic static offsets associated with the April 14 foreshock are shown in Fig. 6a; those for the April 15 foreshock are shown in Fig. 7a with black arrows (for the complete data, see Tables 2 and 3). For comparison, we also show post-processed kinematic positioning results with the IGS final orbit and a higher elevation cut-off angle of 15° to check for the effect of noise due to low elevation satellites (Figs. 6a, 7a; white arrows).

Discrepancies between the extracted coseismic offsets from the real-time and post-processed solutions were less than 2–4 cm, except for the site 1070 during the April 15 foreshock (Fig. 7a). Only the real-time solutions showed a few centimeters of displacement at sites far from the epicenter, which could not be observed in the post-processed solutions (Figs. 6a, 7a). The real-time

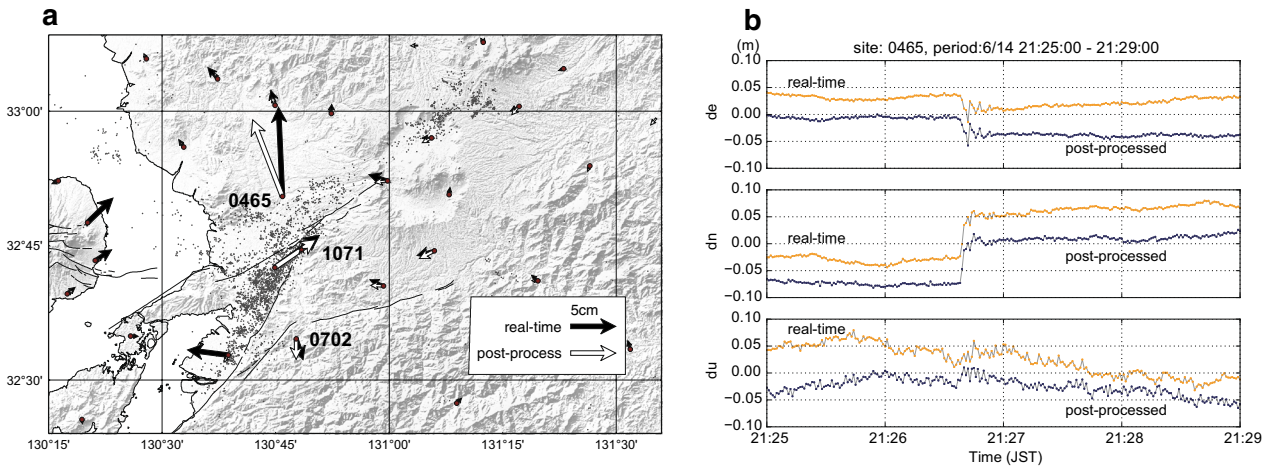

Fig. 6 Coseismic displacements caused by the April 14 foreshock (M_j 6.5). **a** Static coseismic offsets extracted from the GNSS kinematic positioning. *Black arrows* denote the static offsets extracted from real-time positioning results by the REGARD system. *White arrows* denote the static offsets extracted from post-processed GNSS kinematic solutions. The epicenter of the foreshock is shown as a *red star*. The aftershocks in the JMA unified hypocenter catalog between April 14, 2016, and May 18, 2016, are shown by *gray dots*. *Black lines* indicate the ground traces of the active faults. **b** Example of GNSS Kinematic positioning results at site 1071. Upper and bottom time series in *each component* denote the real-time positioning result by the REGARD system and the post-processed GNSS kinematic solution, respectively. The *yellow* and *blue lines* indicate the float solutions and fixed solutions, respectively

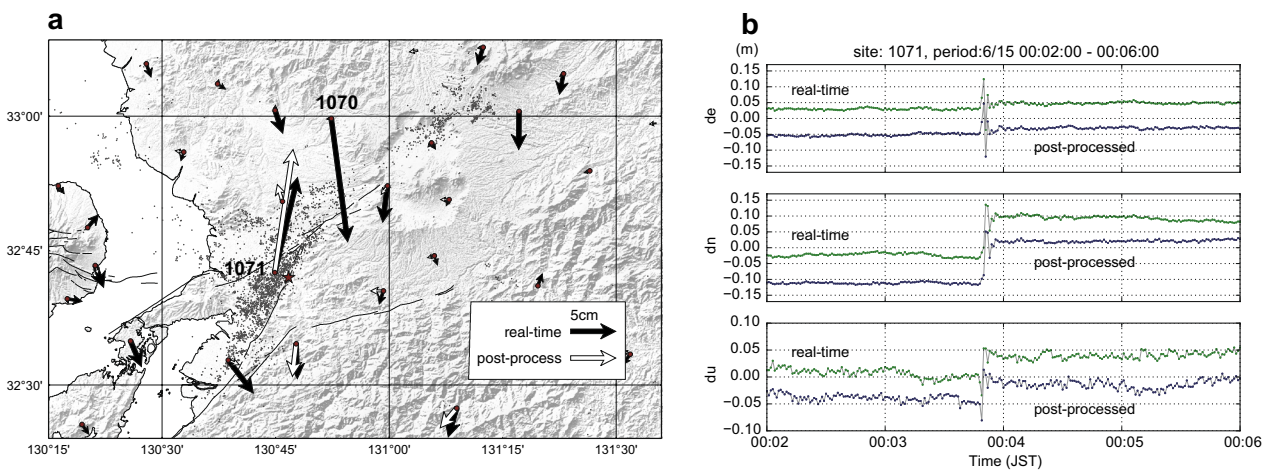

Fig. 7 Coseismic displacements due to the April 15 foreshock (M 6.4). **a** Static coseismic offsets extracted from the GNSS kinematic positioning. *Black arrows* denote the static offsets extracted from real-time positioning results by the REGARD system. *White arrows* denote the static offsets extracted from post-processed GNSS kinematic solutions. The epicenter of the foreshock is shown as a *red star*. The aftershocks in the JMA unified hypocenter catalog between April 14, 2016, and May 18, 2016, are shown as *gray dots*. *Black lines* denote the ground traces of the active faults. **b** Example of GNSS kinematic positioning results at site 1071. Upper and bottom time series in *each component* denote the real-time positioning result by the REGARD system and the post-processed GNSS kinematic solution, respectively. The *green* and *blue lines* indicate the fixed solutions

positioning solutions could be contaminated by delays of data transmission and by multipath noise that cannot be masked with the current low elevation cutoff angle of 7°. The effect of the data delays is the software-specific feature related to RTKLIB 2.4.2 that takes differences of the latest carrier phase data between reference and rover stations ignoring a few seconds of delay in real-time baseline mode. Figure 6b shows the time series of the real-time solution at site 0465 during the April 14 foreshock. Before and after the earthquake, a slight drift of up to a few centimeters is observed in the east component. A similar drift can be observed in the north component at site 1071 after the April 15 foreshock. Although the seismic wave captured by the real-time solutions closely

Table 2 Coseismic displacements caused by the April 14 foreshock (*M* 6.5)

site	Lon. (°)	Lat. (°)	Height (m)	de (cm) real-time	dn (cm) real-time	du (cm) real-time	de (cm) post	dn (cm) post	du (cm) post
0093	130.64560	32.54641	40.4	−4.5	0.6	−1.4	−0.5	−0.8	1.5
0465	130.76479	32.84210	92.27	−0.4	9.9	−6.8	−3.3	8.5	−2.3
0466	131.09930	32.74065	725.32	−1.9	−0.5	1.2	−1.7	−0.9	1.7
0701	130.99622	32.87075	450.81	−2.1	0.7	1.1	−1.4	−0.2	1.7
0702	130.79490	32.57673	287.80	0.8	−2.3	0.6	0.0	−2.3	0.5
0703	131.09342	32.95065	544.65	−1.1	0.0	0.5	−1.0	−0.5	0.4
0704	131.13215	32.84500	650.94	0.1	0.8	−1.7	−0.1	0.4	0.5
1070	130.87266	32,99594	289.97	0.0	1.0	0.5	−0.2	0.5	0.9
1071	130.74837	32.70923	69.51	5.0	3.6	−4.5	4.6	3.1	−4.1
1169	130.98714	32.67516	496.70	−1.5	0.7	−0.8	−1.4	0.1	−0.5

Table 3 Coseismic displacements caused by the April 15 foreshock (*M* 6.4)

site	Lon. (°)	Lat. (°)	Height (m)	de (cm) real-time	dn (cm) real-time	du (cm) real-time	de (cm) post	dn (cm) post	du (cm) post
0093	130.64560	32.54641	40.4	2.8	−3.7	0.4	1.2	−0.5	0.0
0465	130.76479	32.84210	92.27	−0.1	0.7	−0.1	−0.6	1.9	0.0
0466	131.09930	32.74065	725.32	0.4	−1.0	−0.8	−0.7	−0.2	−0.5
0701	130.99622	32.87075	450.81	−0.5	−4.0	1.8	−0.7	−1.0	1.7
0702	130.79490	32.57673	287.80	0.1	−3.9	−1.5	−0.4	−3.6	−2.0
0703	131.09342	32.95065	544.65	0.4	−0.7	−0.7	−0.4	−0.4	0.1
0704	131.13215	32.84500	650.94	−0.3	−0.7	−1.0	−0.9	0.0	−0.4
1070	130.87266	32.99594	289.97	1.8	−13.7	−0.5	−0.5	−0.1	−0.9
1071	130.74837	32.70923	69.51	2.5	10.6	3.5	2.0	13.7	2.5
1169	130.98714	32.67516	496.70	−0.5	−1.5	1.0	−1.4	0.0	−0.7

resembles the post-processed solutions, the slight drifts were not reproduced by the post-processed solutions. Thus, these drifts can be regarded as positioning errors. Moreover, site 1070 shows a large offset of ~14 cm during the April 15 foreshock (Fig. 7a). During the earthquake, the solution of site 1070 switched from a float to a fixed one, indicating that the carrier phase ambiguity was successfully resolved to an integer value from a float value. As a result, this displacement included an offset between the float and fixed solutions; thus, this offset was an apparent rather than a real displacement.

To sum up, significant coseismic displacements caused by the two foreshocks could be detected by the REGARD system. Significant differences between the deformation patterns due to the two foreshocks were observed: For the April 14 event, a maximum horizontal displacement of ~10 cm to the north direction was observed at site 0465, located ~10 km north of the fault segment. On the other hand, for the April 15 event, the maximum horizontal displacement of ~11 cm to the NNE direction was observed at site 1071, which is situated ~5 km south of the junction of the faults. These results imply that the two foreshocks ruptured the northern parts of the Hinagu fault segment, especially the April 15 event ruptured the southern part of the April 14 event. This is in good agreement with the slip distribution model inferred from InSAR analysis by Kobayashi (2016), which shows two main slip patches along the northern part of the Hinagu fault segment. The real-time positioning included larger errors than the post-processed results, and an apparent offset due to the ambiguity resolution result was also observed. To achieve more stable real-time positioning, we will consider a reduction in the data transfer delay, a better choice of elevation cutoff angle, and use of more accurate orbit information.

The detected displacement data of *M*6-class earthquakes (Tables 2, 3) can be used to infer the geometry of earthquake faults and their magnitudes. For a further study on the finite-fault models for these foreshocks, see Yarai et al. (2016).

Simulated real-time fault model estimates for the two foreshocks

As discussed in the previous subsection, significant coseismic displacements were detected in the two large foreshocks by the real-time positioning. An important

question is if the threshold of the magnitude was low enough to detect these foreshocks, how accurately did the REGARD system estimate the finite-fault models? Therefore, we simulated the real-time situations, assuming that the threshold for the JMA EEW is $M > 6$ to trigger the REGARD system.

For the April 14 event (M_j 6.5), the first finite-fault model was derived at 38 s with M_w 5.94 and was updated to 6.11 at 50 s. Finally, the finite-fault model converged with M_w 6.12 at 1 m 32 s, which is roughly consistent with the CMT solution by JMA (M_w 6.2). The estimated fault was, however, an auxiliary fault plane of the Hinagu fault (Additional file 3: Figure S3). The residual was also large (VR 27.9%) compared with the mainshock case (Table 1) because the signal-to-noise ratios in almost all of the stations were small. For the April 15 event (M_j 6.4), the first finite-fault model was derived at 1 m 7 s with M_w 5.50 and not subsequently updated (Additional file 4: Figure S4). The displacement at station 1071 was well explained by the model; however, the estimated width was very short compared with the real fault. In this inversion, the model strongly depended on the a priori parameters and the displacement at station 1071, which is the only near-field station that observed a significant displacement. As discussed in the previous section, the displacement at station 1070 during the April 15 foreshock was apparent offset due to the switch from a floating to a fixed-integer solution.

Based on these trial simulations, the REGARD system could estimate the size of an $M6$-class earthquake approximately within 1 min. However, stable estimation of all the fault parameters for a rectangular fault is difficult because of the lack of near-field stations with high signal-to-noise ratio. The freedom of the model can be decreased using more general a priori information such as a CMT solution that provides the centroid location and the mechanism of the earthquake. One possible implementation is the method proposed by Crowell et al. (2016). This is a topic that is left for future work on the REGARD system.

Conclusions

The REGARD system successfully estimated a single rectangular fault model using RTK-GNSS positioning for the 2016 Kumamoto earthquake (M_j 7.3) within 1 min from the event origin for the first estimation and converged to the appropriate fault plane within an additional 4 min. This is the first operational result of the REGARD system and demonstrates its reaction to a large earthquake in real time since the launch of the prototype system in 2012. The finite-fault estimate with M_w 6.96 was consistent with both the fault models of Yarai et al. (2016), which is inferred from static offsets observed by post-processed GNSS positioning and InSAR analysis, and the JMA CMT solution (JMA 2016c). This result demonstrates that the REGARD system is capable of modeling inland intraplate earthquakes as well as large interplate earthquakes. Thus, the result demonstrates the potential for a GPS-based EEW system in Japan.

The real-time kinematic positioning results show the significant coseismic displacements due to the April 14 and the April 15 foreshocks at sites 0465, 1071, and 0702 with different deformation patterns, implying that the first foreshock ruptured a northern part of the Hinagu fault segment, after which the neighboring south region was ruptured by the second foreshock. Although the finite-fault model inversions were not carried out for these events in real time because the JMA EEW was not exceeded the threshold value in REGARD, the observed coseismic displacements could be still important information for rapid investigations of fault geometry.

Although there are still several issues to be improved, finite-fault estimates are important information for understanding possible damage situations in a timely fashion. Furthermore, the finite-fault estimates can be used to prevent secondary disasters such as seismically triggered landslides that are approximately correlated with the spatial distance from the earthquake source. Future work will involve the development of an inversion routine as well as more stable real-time positioning for more accurate and robust finite-fault estimation. Specifically, use of more accurate a priori information such as rapid CMT solutions based on the seismic and/or the geodetic data will be key approach to improved modeling of inland earthquakes.

Additional files

Additional file 1: Figure S1. Update history of the finite-fault models estimated by the REGARD system during the 2016 Kumamoto earthquake (M_j 7.3) from top to bottom. Observed (black arrows) and predicted (white arrows) displacements for horizontal (left) and vertical (right) components are shown. The red rectangle represents the estimated fault plane, and the blue arrow shows the slip vector. The epicenter of the mainshock is shown as a red star. The aftershocks in the JMA unified hypocenter catalog between April 14, 2016, and May 18, 2016, are shown as gray dots. Black lines indicate the ground traces of the active faults (HERP 2013).

Additional file 2: Figure S2. Same as Figure 4, but for the displacements predicted by a priori model. The a priori model is shown as gray line. Gray arrows denote the displacements predicted by a priori model. The initial VR due to the a priori model is -90.9%.

Additional file 3: Figure S3. Simulated update history of the finite-fault models estimated by the REGARD system during the April 14 foreshock (M_j 6.5) from top to bottom. Observed (black arrows) and predicted (white arrows) displacements for horizontal (left) and vertical (right) components are shown. Gray arrows denote the displacements predicted by a priori model. The red rectangle represents the estimated fault plane, and the blue arrow shows the slip vector. The epicenter of the April 14 foreshock (M_j 6.5) is shown as a red star. The aftershocks in the JMA unified hypocenter catalog between April 14, 2016, and May 18, 2016, are shown as gray dots. Black lines indicate the ground traces of the active faults (HERP 2013). The model parameters are shown in the table at bottom.

Additional file 4: Figure S4. Simulated update history of the finite-fault models estimated by the REGARD system during the April 15 foreshock (M_j 6.4). Observed (black arrows) and predicted (white arrows) displacements for horizontal (left) and vertical (right) components are shown. Gray arrows denote the displacements predicted by a priori model. The red rectangle represents the estimated fault plane, and the blue arrow shows the slip vector. The epicenter of the April 15 foreshock (M_j 6.4) is shown as a red star. The aftershocks in the JMA unified hypocenter catalog between April 14, 2016, and May 18, 2016, are shown as gray dots. Black lines indicate the ground traces of the active faults (HERP 2013). The model parameters are shown in the table at bottom. The finite-fault model was not updated after the first model in this test.

Abbreviations

EEW: Earthquake Early Warning of JMA; GEONET: GNSS Earth Observation Network System; GNSS: Global Navigation Satellite System; GPS: global positioning system; GSI: Geospatial Information Authority of Japan; JMA: Japan Meteorological Agency; HERP: Earthquake Research Committee, Headquarters for Earthquake Research Promotion; REGARD: the Real-time GEONET Analysis System for Rapid Deformation monitoring; RTK: real-time kinematic; VR: variance reduction.

Authors' contributions

SK drafted the manuscript. YH, YO, and TN revised the manuscript. All authors read and approved the final manuscript.

Author details

[1] Geodetic Observation Center, Geospatial Information Authority of Japan, 1 Kitasato, Tsukuba, Japan. [2] Research Center for Prediction of Earthquakes and Volcanic Eruptions, Graduate School of Science, Tohoku University, Sendai, Japan. [3] Disaster Prevention Research Institute, Kyoto University, Uji, Japan.

Acknowledgements

The authors are indebted to GSI colleagues for the operation of the REGARD system. The authors thank the Japan Meteorological Agency (JMA) for providing the earthquake catalog and the International GNSS Service (IGS) for providing the products used in this study. RTKLIB 2.4.2 software (Takasu 2013) was used for the GNSS analysis. Figures are drawn using Generic Mapping Tools (Wessel and Smith 1998) and matplotlib (Hunter 2007). We also acknowledge the comments by Yehuda Bock and an anonymous reviewer in improving the manuscript. This work was partly supported by Japan Society for the Promotion of Science (JSPS) KAKENHI Grant Number 15H03713.

Competing interests

The authors declare that they have no competing interests.

Received: 11 July 2016 Accepted: 5 November 2016
Published online: 22 November 2016

References

Blewitt G, Hammond WC, Kreemer C, Plag HP, Stein S, Okal E (2009) GPS for real-time earthquake source determination and tsunami warning systems. J Geodesy 83(3–4):335–343. doi:10.1007/s00190-008-0262-5

Bock Y, Melgar D, Crowell W (2011) Real-time strong-motion broadband displacements from collocated GPS and accelerometers. Bull Seismol Soc Am 101(6):2904–2925. doi:10.1785/0120110007

Cabinet Office, Government of Japan (2016) Damage situation associated with the earthquake in the Kumamoto region (as of June 16, 17:15). http://www.bousai.go.jp/updates/h280414jishin/pdf/h280414jishin_31.pdf. Accessed 18 June 2016 **(in Japanese)**

Crowell BW, Bock Y, Melgar D (2012) Real-time inversion of GPS data for finite fault modeling and rapid hazard assessment. Geophys Res Lett 39:L09305. doi:10.1029/2012GL051318

Crowell BW, Schmidt DA, Bodin P, Vidale JE, Gomberg J, Hartog JR, Kress VC, Melbourne TI, Santillan M, Minson SE, Jamison DG (2016) Demonstration of the Cascadia G-FAST geodetic earthquake early warning system for the Nisqually, Washington, Earthquake. SRL 87(4):930–943. doi:10.1785/0220150255

Geng J, Bock Y, Melgar D, Crowell BW, Haase JS (2013) A new seismogeodetic approach applied to GPS and accelerometer observations of the 2012 Brawley seismic swarm: implications for earthquake early warning. Geochem Geophys Geosyst 14(7):2124–2142. doi:10.1002/ggge.20144

Grapenthin R, Johanson IA, Allen RM (2014) Operational real-time GPS-enhanced earthquake early warning. J Geophys Res Solid Earth 119:7944–7965. doi:10.1002/2014JB011400

Headquarters for Earthquake Research Promotion (2013) Long-term evaluation of the Futagawa and Hinagu fault zones (2013 revision). http://jishin.go.jp/main/chousa/katsudansou_pdf/93_futagawa_hinagu_2.pdf. Accessed 21 June 2016 **(in Japanese)**

Headquarters for Earthquake Research Promotion (2016) Evaluation of the 2016 Kumamoto Earthquakes. http://www.jishin.go.jp/main/chousa/16may_kumamoto/index-e.htm. Accessed 18 June 2016

Hoshiba M, Kamigaichi O, Saito M, Tsukada S, Hamada N (2008) Earthquake early warning starts nationwide in Japan. EOS Trans AGU 89:73–74. doi:10.1029/2008EO080001

Hunter JD (2007) Matplotlib: a 2D graphics environment. Comput Sci Eng 9(3):90–95. doi:10.1109/MCSE.2007.55

Japan Meteorological Agency (2016a) The 2016 Kumamoto Earthquake -Portal-. http://www.jma.go.jp/jma/en/2016_Kumamoto_Earthquake/2016_Kumamoto_Earthquake.html. Accessed 18 June 2016

Japan Meteorological Agency (2016b) Content of earthquake early warnings. http://www.data.jma.go.jp/svd/eew/data/nc/pub_hist/2016/04/20160416012510/content/content_out.html. Accessed 21 June 2016 **(in Japanese)**

Japan Meteorological Agency (2016c) CMT solution list. http://www.data.jma.go.jp/svd/eqev/data/mech/cmt/fig/cmt20160416012505.html. Accessed 19 June 2016

Kawamoto S, Miyagawa K, Yahagi T, Todoriki M, Nishimura T, Ohta Y, Hino R, Miura S (2015) Development and assessment of real-time fault model estimation routines in the GEONET real-time processing system. Int Assoc Geod Symp. doi:10.1007/1345_2015_49

Kobayashi T (2016) Seismic slip properties for foreshocks of the 2016 Kumamoto Earthquake revealed by InSAR analyses. In: Paper presented at the Seismological Society of Japan Fall Meeting 2016, The Nagoya Congress Center, Nagoya, 5–7 Oct 2016 **(in Japanese)**

Kobayashi T, Ohta Y, Miura S, Hino R, Fujimoto H, Demachi T, Tachibana K (2012) Improvement on automatic detection method of coseismic displacement in the RTK-GPS time series using neighboring sites information. J Geod Soc Jpn 58(2):77–87. doi:10.11366/sokuchi.58.77 **(in Japanese with English abstruct)**

Kouba J (2009) A guide to using international GNSS service (IGS) products. https://igscb.jpl.nasa.gov/components/usage.html. Accessed 18 June 2016

Matsu'ura M, Hasegawa Y (1987) A maximum likelihood approach to nonlinear inversion under constraints. Phys Earth Planet Inter 47:179–187. doi:10.1016/0031-9201(87)90076-8

Melgar D, Bock Y (2013) Near-field tsunami models with rapid earthquake source inversions from land and ocean based observations: the potential for forecast and warning. J Geophys Res 118:5939–5955. doi:10.1002/2013JB010506

Melgar D, Bock Y (2015) Kinematic earthquake source inversion and tsunami runup prediction with regional geophysical data. J Geophys Res Solid Earth 120:3324–3349. doi:10.1002/2014JB011832

Melgar D, Crowell BW, Bock Y, Haase JS (2013) Rapid modeling of the 2011 Mw 9.0 Tohoku-oki earthquake with seismogeodesy. Geophys Res Lett 40:2963–2968. doi:10.1002/grl.50590

Melgar D, Geng J, Crowell BW, Haase JS, Bock Y, Hammond WC, Allen RM (2015) Seismogeodesy of the 2014 Mw 6.1 Napa earthquake, California: rapid response and modeling of fast rupture on a dipping strike-slip fault. J Geophys Res Solid Earth 120:5013–5033. doi:10.1002/2015JB011921

Minson SE, Murray JR, Langbein JO, Gomberg JS (2014) Real-time inversions for finite fault slip models and rupture geometry based on high-rate GPS data. J Geophys Res Solid Earth 119:3201–3231. doi:10.1002/2013JB010622

Nakagawa H, Toyofuku T, Kotani K, Miyahara B, Iwashita C, Kawamoto S, Hatanaka Y, Munekane H, Ishimoto M, Yutsudo T, Ishikura N, Sugawara Y (2009) Development and validation of GEONET new analysis strategy (Version 4). J Geospatial Inf Auth Jpn 118:1–8 **(in Japanese)**

Ohta Y, Kobayashi T, Tsushima H, Miura S, Hino R, Takasu T, Fujimoto H, Iinuma T, Tachibana K, Demachi T, Sato T, Ohzono M, Umino N (2012) Quasi real-time fault model estimation for near-field tsunami forecasting based on RTK-GPS analysis: application to the 2011 Tohoku-Oki earthquake (Mw 9.0). J Geophys Res Solid Earth (1978–2012) 117(B2):B02311. doi:10.1029/2011JB008750

Ohta Y, Kobayashi T, Hino R, Demachi T, Miura S (2015) Rapid coseismic fault determination of consecutive large interplate earthquakes: the 2011 Tohoku-Oki sequence. Int Assoc Geod Symp. doi:10.1007/1345_2015_109

Okada Y (1992) Internal deformation due to shear and tensile faults in a half-space. Bull Seismol Soc Am 82(2):1018–1040

Takasu T (2013) RTKLIB: an open source program package for GNSS positioning. http://www.rtklib.com. Accessed 18 June 2016

Terakawa T, Matsu'ura M (2009) A methodological breakthrough in stress inversion: estimation of 3-D tectonic stress patterns from CMT data inversion. Zisin (J Seismol Soc Jpn) 2:339–346. doi:10.4294/zisin.61.339 **(in Japanese with English abstract)**

Utsu T (2001) Jishingaku 3rd edn. Kyoritsu Shuppan **(in Japanese)**

Wessel P, Smith WHF (1998) New, improved version of generic mapping tools released. EOS Trans AGU 79(47):579. doi:10.1029/98EO00426

Yarai H, Kobayashi T, Morishita Y, Fujiwara S, Munekane H, Hiyama Y, Kawamoto S, Miyahara B, SAR Analysis Group, GEONET Analysis Group (2016) Crustal deformation of the 2016 Kumamoto Earthquake. In: Paper presented at Japan Geoscience Union Meeting 2016, Makuhari Messe, Chiba, 22–26 May 2016